Research Article

Mohamed Zayed, Mervat Nasr, Mamduh J. Aljaafreh*, Mohammad Marashdeh, M. Al-Hmoud, Mohamed Shaban, Mohamed Rabia, Amna Tarek, and Ashour M. Ahmed*

Sodium titanium oxide/zinc oxide (STO/ZnO) photocomposites for efficient dye degradation applications

https://doi.org/10.1515/gps-2023-0272
received December 29, 2023; accepted May 06, 2024

Abstract: In this study, sodium titanium oxide ($Na_2Ti_3O_7$, termed STO) and sodium titanate/zinc oxide (STO/ZnO) photocomposites were prepared for the first time. A low-cost hydrothermal technique was employed to fabricate the STO/ZnO photocomposites with varying ZnO weight ratios: STO/0.25ZnO, STO/0.5ZnO, and STO/ZnO. The prepared photocomposites were investigated for the decomposition of methylene blue dye (MB) under natural visible light illumination and an artificial tungsten halogen lamp. The STO/ZnO photocomposite exhibits high photodegradation performance, which can be correlated with its properties and characterization. The X-ray diffraction analysis reveals that STO has an average crystallite size of 69.1 nm, ZnO has an average crystallite size of 41.4 nm, and the combination of STO/ZnO results in a reduced average crystallite size of 39.5 nm. The bandgap (E_g) of STO/ZnO is 2.53 eV after controlling the ZnO weight ratio. The photocatalytic efficiency of the STO/ZnO photocomposite was 100% for MB within 60 min of solar light irradiation, compared to 33.7% for STO and 25.8% for ZnO. The effect of STO/ZnO dosage and MB concentration was investigated. Furthermore, the kinetics and mechanisms of the photocatalytic process were examined. The results suggest that STO/ZnO has promising potential for practical applications in wastewater treatment.

Keywords: sodium titanium oxide, zinc oxide, energy gap, photocatalytic degradation, organic dye

*** Corresponding author: Mamduh J. Aljaafreh**, Physics Department, College of Science, Imam Mohammad Ibn Saud Islamic University (IMSIU), Riyadh, 11623, Saudi Arabia, e-mail: maljaafreh@imamu.edu.sa
*** Corresponding author: Ashour M. Ahmed**, Physics Department, College of Science, Imam Mohammad Ibn Saud Islamic University (IMSIU), Riyadh, 11623, Saudi Arabia; Nanophotonics and Applications Lab, Physics Department, Faculty of Science, Beni-Suef University, Beni-Suef 62514, Egypt, e-mail: asmmohamed@imamu.edu.sa
Mohamed Zayed: Nanophotonics and Applications Lab, Physics Department, Faculty of Science, Beni-Suef University, Beni-Suef 62514, Egypt
Mervat Nasr: Nanophotonics and Applications Lab, Physics Department, Faculty of Science, Beni-Suef University, Beni-Suef 62514, Egypt; Chemistry Department, Faculty of Science, Beni-Suef University, Beni-Suef 62514, Egypt
Mohammad Marashdeh, M. Al-Hmoud: Physics Department, College of Science, Imam Mohammad Ibn Saud Islamic University (IMSIU), Riyadh, 11623, Saudi Arabia
Mohamed Shaban: Nanophotonics and Applications Lab, Physics Department, Faculty of Science, Beni-Suef University, Beni-Suef 62514, Egypt; Department of Physics, Faculty of Science, Islamic University of Madinah, P.O. Box 170, AlMadinah Almonawara 42351, Saudi Arabia
Mohamed Rabia: Nanophotonics and Applications Lab, Physics Department, Faculty of Science, Beni-Suef University, Beni-Suef 62514, Egypt; Nanomaterials Science Research Laboratory, Chemistry Department, Faculty of Science, Beni-Suef University, Beni-Suef, 62514, Egypt
Amna Tarek: Chemistry Department, Faculty of Science, Beni-Suef University, Beni-Suef 62514, Egypt

1 Introduction

Today, the widespread use of organic dyes in various industries, including textiles, paper, plastics, and other materials, has significantly contributed to water pollution [1]. Approximately 200,000 tons of dyes are lost every year without undergoing wastewater treatment processes [2]. These dyes pose multiple threats to the environment and human health as they release dangerous and carcinogenic compounds during their breakdown [3,4]. The persistence of organic dyes in soil and water for long periods is harmful to living microorganisms and reduces agricultural productivity. Moreover, they disrupt the absorption and scattering of sunlight, which is vital for photosynthesis in aquatic plants and the growth of algae. Therefore, the study of dye-polluted water is indeed crucial for understanding the extent of water pollution. Among these dyes, methylene blue (MB) poses a severe threat to both human

and aquatic life when it contaminates water sources [5]. Ingesting MB can cause various health issues, including cyanosis, jaundice, rapid heartbeat, nausea, and methemoglobinemia [6]. Moreover, it has been identified as highly carcinogenic and capable of promoting the growth of malignant cells. The development of eco-friendly and cost-effective methods for removing MB dye from wastewater has received significant attention worldwide [7]. Various techniques, such as membrane filtering, photocatalytic degradation, advanced oxidation, liquid–liquid extraction, ozonation, adsorption, and biosorption, have been employed to treat wastewater containing dyes [8–10]. Recently, there has been a significant interest in utilizing solar energy for the degradation of pollutants through photocatalytic reduction, as a means to address the environmental cleanup of harmful substances [11]. The utilization of sunlight as an illuminating source for diverse photocatalytic reactions has experienced remarkable growth due to its abundance, sustainability, clean energy status, and wide range of wavelengths. During photocatalytic reactions, photocatalysts utilize photo-induced electron–hole pairs (e^-/h^+) on their surface when exposed to sunlight. These pairs can generate various reactive species, including hydroxyl radicals ($OH^\bullet$) and superoxide radicals ($O_2^{\cdot-}$). The reactive species effectively attack the chemical bonds within dye molecules through oxidation and reduction reactions. This leads to the breakdown of complex organic dyes into smaller fragments and their ultimate conversion into water and carbon dioxide. As a result, MB dye is transformed into safe by-products. Therefore, the photocatalytic process represents an innovative and eco-friendly technique for water treatment. Moreover, it offers numerous advantages, such as high efficiency, operation at room temperature, low cost, and no production of secondary waste [12].

Up to now, many semiconductor nanomaterials, such as titanium dioxide (TiO_2) nanoparticles [13], molybdenum disulfide (MoS_2) nanosheets [14] carbon nanotubes [15], and graphene [16], have been employed as photocatalysts for dye removal. Alkali titanate nanomaterials, which are p-type semiconductors, have drawn considerable interest due to their potential applications. The alkali titanates materials are described by the general formula $A_2O{\cdot}nTiO_2$ or $A_2Ti_nO_{2n+1}$ (A = Na, K, or Cs, and $3 \le n \le 8$) [17]. Among different alkali titanates, sodium titanium oxide ($Na_2Ti_3O_7$, termed STO) or disodium tri-titanate has gained greater attention in recent years. The structure of $Na_2Ti_3O_7$ is made up of layers of negatively charged ions $(Ti_3O_7)^{2-}$ [18,19]. The layers of $(Ti_3O_7)^{2-}$ are stacked on top of each other, and each layer is joined together at the corners. $(Ti_3O_7)^{2-}$ ions are held together by positively charged sodium ions (Na^+) located at the pseudo-cubic sites. The terminal oxygen atoms in $(Ti_3O_7)^{2-}$ ions are coordinated to only one (TiO_6) octahedron. STO has a high surface area, easy to control microstructures, and good chemical stability [20–22]. $Na_2Ti_3O_7$ is a promising ferroelectric material with good absorption in the range in the ultraviolet (UV) region [23]. Also, $Na_2Ti_3O_7$ offers large basic sites due to the presence of two lone pair electrons on the oxygen atom, which makes it suitable for ion exchange and facilitates the adsorption onto the material's surface [24–26]. The alkali ions carrying charge are present in the interlayer space between the titanate layers and can be interchanged with other cations [27]. Also, the ions exchangeable with ionic species can create interband states in their electronic structure, which improves photo-responsiveness [28]. A hydrothermal approach of TiO_2/NaOH, solid-state reactions of TiO_2/Na_2CO_3, and sol-gel process of $Ti(C_3H_7O)_4$/NaOH are employed for the synthesis of $Na_2Ti_3O_7$ [29,30].

Unfortunately, the photocatalytic activity of STO is relatively limited [31]. This is because STO has many drawbacks, such as high E_g and low visible light absorption. Therefore, tremendous efforts have been undertaken to increase the photoactivity of STO. For instance, Teng et al. reported that the Sn-STO nanotubes achieved 52% MB photodegradation after 270 min of visible-light irradiation [32]. Feng et al. prepared sodium titanate layers with flower-like structures by hydrothermal technique in a weakly alkaline medium [33]. The resulting nanomaterials exhibited low photodegradation properties. After more than 120 min of reaction, complete photodegradation of MB (100%) was achieved. Jiang et al. evaluated the photocatalytic activity of $Na_2Ti_3O_7$ for the photodegradation of MB under visible-light irradiation [34]. They reached 100% efficiency after 4 h. In a study by Vithal et al., Cu^{2+}- and Ag^+-doped forms of $Na_2Ti_3O_7$ were fabricated using the ion-exchange method [35]. The Ag^+-doped $Na_2Ti_3O_7$ displayed significant photocatalytic activity in the photodegradation of MB dye under visible-light irradiation. After 120 min, the percentage of MB degradation was observed to be 90% for Ag-STO.

Recently, there has been a growing interest in the formation of heterojunctions between two or more semiconductor materials to enhance the efficiency of photocatalytic systems [36,37]. This approach enables more efficient charge transfer and assists in the separation of photogenerated electron–hole pairs, owing to the synergistic effects [38,39]. The limitations of the recombination of electron–hole pairs before their participation in photocatalytic reactions can be overcome by introducing engineering defects on the surface of heterogeneous photocatalysts. These defects play a crucial role in enhancing the photocatalytic efficiency. By introducing defects, several benefits can be achieved, including improved light absorption, facilitated charge separation,

reduced electron–hole recombination, modulation of the electronic structure, and the generation of reactive radicals [40].

However, zinc oxide (ZnO) has lately become one of the most studied multifunctional n-type semiconductors due to its properties. ZnO exhibits a wide bandgap, high exciton binding energy, excellent electron mobility, remarkable redox potential, superior quantum efficiency, substantial conductivity, and outstanding stability [41,42]. These characteristics make ZnO a promising material for various applications in optoelectronics, sensors, and energy devices. Regrettably, ZnO is limited in its practical applications for photocatalysis due to its wide band gap, high electron/hole recombination rate, and low photostability. This study seeks to fabricate ZnO, STO, and STO/*x*ZnO photocatalysts through a combination of a simple hydrothermal method and a physical mixing solid–solid process to enhance efficiency in dye degradation applications. The effects of the ZnO weight ratio loaded over STO on the structure, morphology, chemical composition, and optical properties have been examined. The effect of the STO/*x*ZnO photocomposite via photocatalytic MB dye degradation has been studied under a tungsten halogen lamp and sunlight. The photodegradation process's kinetics, stability, and mechanism were considered and explained in detail. To our knowledge, there are no studies on the characteristics of STO combined with ZnO nanoparticles and their application in photocatalysis.

2 Materials and methods

2.1 Fabrication of sodium titanate (STO) nanoparticles

STO nanoparticles have been fabricated by a simple and low-cost hydrothermal alkaline technique [43]. To initiate the hydrothermal reaction, approximately 5 g of TiO_2 powder (99.7%, Sigma-Aldrich) was mixed with 200 mL of 10 M NaOH solution (98%, Sinopharm Chemical Reagent Co.). The resulting mixture was stirred using a magnetic stirrer (RTC-2, Gongyi Yuhua Instrument Co.) for 30 min until a white suspension solution was obtained. Subsequently, the suspension solution was transferred to a 1 L Teflon autoclave. The hydrothermal treatment was conducted at 140°C in a muffle furnace (F3043, Thermo Fisher Scientific Co.) for 20 h. After the hydrothermal reaction is completed, the stainless steel autoclave is left to cool at room temperature. Then, to get rid of the unreacted NaOH, the obtained white precipitate was separated, filtered, and washed several times with distilled water (DW). Finally, the resultant white STO nanoparticle was dried in an oven (BOV-V230F, Biobase Biozone Co.) at 70°C for 12 h.

2.2 Synthesis of ZnO nanoparticles

ZnO nanoparticles have been fabricated using a hydrothermal process [44]. Briefly, 0.1 M of zinc acetate ($Zn(CH_3CO_2)_2{\cdot}6H_2O$) (99.9%, Kojundo Chemical Lab. Co.) was dissolved in 400 mL of DW under a vigorous stirrer for 1 h to get a more homogenous white solution. Subsequently, the pH of the solution was adjusted to 10 by gradually adding 5 M NaOH aqueous solution drop by drop. Then, the mixture was placed in a 1 L Teflon autoclave at 170°C for 10 h in a muffle furnace to perform the hydrothermal process reaction. After that, the obtained white precipitate was washed with DW several times. Finally, the resultant white ZnO nanoparticle was dried at 90°C for 6 h followed by calcination at 300°C for 3 h.

2.3 Fabrication of STO/ZnO photocomposites

Three different ZnO/STO photocomposites were prepared using a thorough physical solid–solid process involving ZnO and STO nanoparticles. Various weight ratios of ZnO nanoparticles (0.25, 0.5, and 1 g) were separately mixed with 1 g of STO nanoparticles at room temperature. Initially, the mixture was pounded together in a mortar for 10 min to ensure proper blending. Subsequently, the mixed STO and ZnO nanoparticles were subjected to ultrasonic dispersal in 50 mL of DW for 1 h, followed by stirring for 3 h to achieve an aqueous dispersion. After the dispersion process, the mixture was filtered, and the resulting nanoparticle precipitation was collected. The collected precipitate was then dried for 12 h at 80°C. The final obtained nanoparticles were labeled as STO/*x*ZnO, where '*x*' represents the different weights of ZnO loaded (0.25, 0.5, and 1).

2.4 Characterization techniques

The surface morphologies of nanoparticles were examined using a scanning electron microscopy (SEM; JEOL, JSM-5410LV, Japan) device. The attached energy-dispersive X-ray (EDX) unit with an SEM device was utilized to identify the composition and quantitative ratios of the fabricated

nanoparticles. The structural and phase analysis was studied using X-ray diffraction (XRD; Philips X'Pert Pro MRD) with a Cu-K radiation source (λ = 0.154 nm) at 40 kV. The XRD data were collected with a step interval of 0.01° in the range of 5–70°. A PerkinElmer (Lambda) spectrophotometer was used to investigate the optical characteristics of the nanoparticles. The surface characteristics and pore sizes of STO, ZnO, and STO/ZnO were analyzed using the Brunauer–Emmett–Teller (BET) technique, specifically employing Micromeritics Gemini 2375 and Gemini V instruments.

2.5 Photocatalytic measurements

The photocatalytic performance of the fabricated STO, ZnO, and STO/*x*ZnO was evaluated for the degradation of MB dye, serving as a model pollutant, under a 400-W tubular tungsten halogen lamp (500 W JTT, Janta Light House) and sunlight irradiation. The initial MB dye conditions were 5 ppm concentration, 50 mL volume, and pH 7 at room temperature. Before the photocatalytic reaction, the mixture was stirred for 30 min in the dark to ensure adsorption–desorption equilibrium. Following that, the nanoparticles of the solution were obtained at regular intervals for up to an hour and then used to determine the absorbance at a wavelength range of 600–700 nm. The photocomposite dose, illumination duration, and starting MB concentration were measured. Additionally, during five photodegradation tests at varying exposure times, the stability of the photocomposite was examined. The levels of total organic carbon (TOC) were measured using a TOC analyzer instrument (Sievers InnovOx ES). Electrochemical impedance spectroscopy (EIS) was performed in 0.5 M Na_2SO_4 electrolyte using OrigaFlex potentiostat (OrigaLys ElectroChem., OGF01A) device.

3 Results and discussion

3.1 Characterization of the prepared nanoparticles

3.1.1 XRD of the fabricated nanoparticles

The crystal structure and phase of STO, ZnO, and STO/ZnO nanoparticles were characterized, as displayed in Figure 1. The XRD pattern of STO matched with the monoclinic $Na_2Ti_3O_7$ phase (card No. JCPDS 96-231-0332, space group *P*121/*m*1) [43,45]. The basic characteristic diffraction peaks of monoclinic STO located at 2θ = 10.42, 34.17, 34.52, 35.24, 38.11, 39.92, and 40.02° were related to Miller indices (100), ($\bar{3}$02), (211), ($\bar{2}$12), ($\bar{1}$13), (310), and (004), respectively. The XRD spectrum, Figure 1(b), confirms the hexagonal phase structure of ZnO with a space group P 63 mc according to card No. JCPDS 96-900-8878 [46,47]. The main characteristic peaks were positioned at 2θ = 31.79, 34.42, 36.29, 47.52, 56.54, 62.83, 66.31, 67.87, 69.01, 72.55, 77.01, and 81.32°. These peaks were associated with the Miller planes (100), (002), (101), (102), (110), (103), (200), (112), (201), (004), (202), and (104), respectively. The STO/ZnO photocomposite showed no extra diffraction peaks, as seen in Figure 1(c). The intensities of the diffraction peaks of STO were reduced with peaks shift position after the incorporation of ZnO (Figure 1(d)).

Table S1 displays several important XRD structural parameters, including the texture coefficient (TC), crystallite size (D), and dislocation density (δ). The average crystallite sizes (D) for STO, ZnO, and STO/ZnO nanoparticles were determined using Scherrer's equation [48,49]:

$$D = \frac{0.94\lambda}{\beta \cos \theta} \quad (1)$$

Here, the full half-width maximum (β) is derived from the XRD data, and λ represents the wavelength of the Cu-K radiation source (0.154 nm). A broader peak corresponds to a smaller crystallite size. The average crystallite size was approximately 69.1 nm for STO and 41.4 nm for ZnO. Interestingly, the average crystallite size of STO/ZnO decreased to 39.5 nm. This reduction can be attributed to the creation of additional nucleating centers, which lowers the nucleation energy barrier [50].

When a nanoparticle undergoes deformation, it introduces a lattice distortion known as macrostrain, resulting in the broadening of diffraction peaks. The XRD peak width is primarily influenced by both the size and microstrain in the nanoparticle. The Scherrer equation only accounts for the size effect and does not consider microstrain in peak broadening. To evaluate the microstrain and size, the Williamson–Hall (W–H) model was employed [6,51]:

$$\beta \cos \theta = \frac{0.94\lambda}{D} + 4\varepsilon \sin\theta \quad (2)$$

If the microstrain approaches zero or has a very small value ($\varepsilon \approx 0$) in the W–H equation, it simplifies to the Scherrer equation. Plotting the values of $\beta \cos\theta$ against 4 $\sin\theta$ in a standard W–H plot yields a linear fitting curve, as depicted in Figure 2. The intercept and slope of the fitting line correspond to the average crystallite size (D) and microstrain (ε), respectively. Positive and negative slope values indicate tensile and compressive strains, respectively. The fabricated nanoparticles of STO, ZnO, and STO/ZnO exhibited average crystallite sizes of 43.9, 55.9, and 66.4 nm,

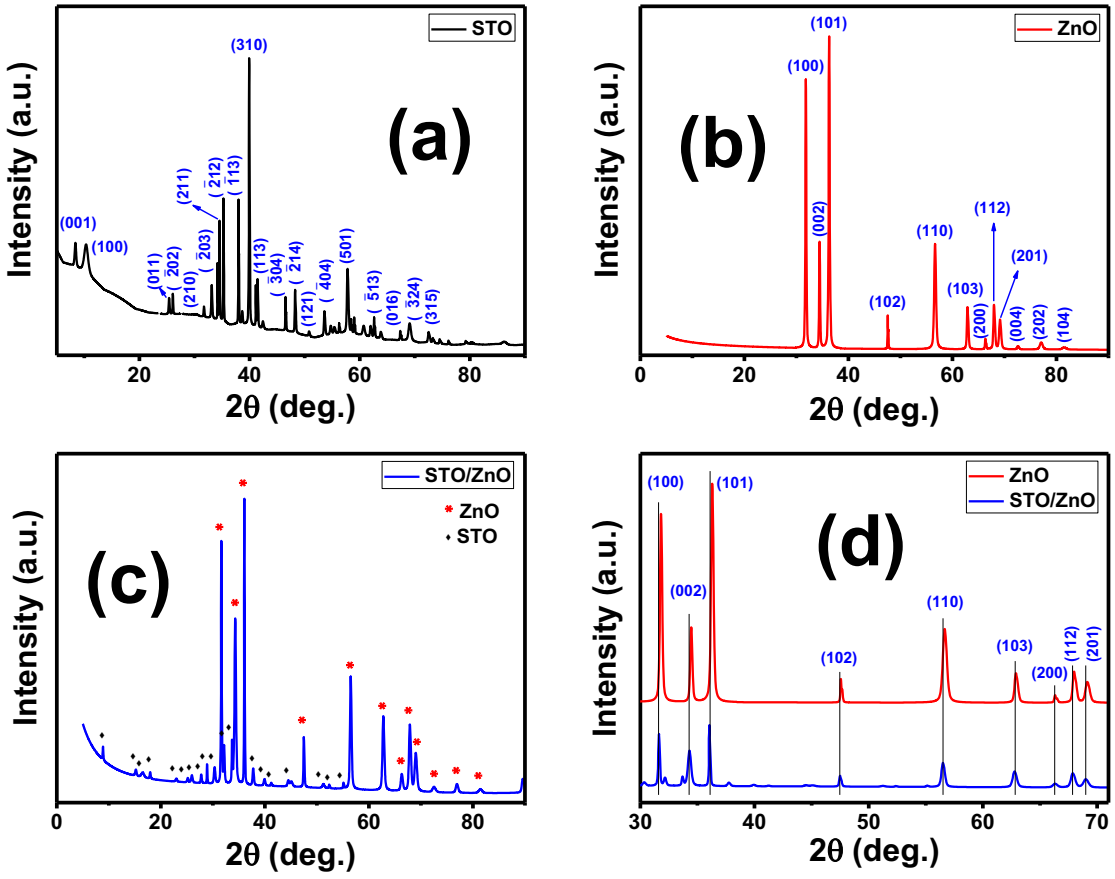

Figure 1: XRD patterns of (a) STO, (b) ZnO, (c) STO/ZnO, and (d) peak shifts of ZnO and STO/ZnO after ZnO loading.

respectively. In terms of microstrain, the values were –2.16 × 10^{-4}, –1.20 × 10^{-4}, and 21.8 × 10^{-4} for STO, ZnO, and STO/ZnO, respectively.

TC and δ were calculated using the following equations [52,53]:

$$\mathrm{TC}(hkl) = \frac{1}{N} \times \frac{I(hkl)/I_0(hkl)}{\left[\sum \frac{I(hkl)}{I_0(hkl)}\right]} \tag{3}$$

$$\delta = \frac{1}{D^2} \tag{4}$$

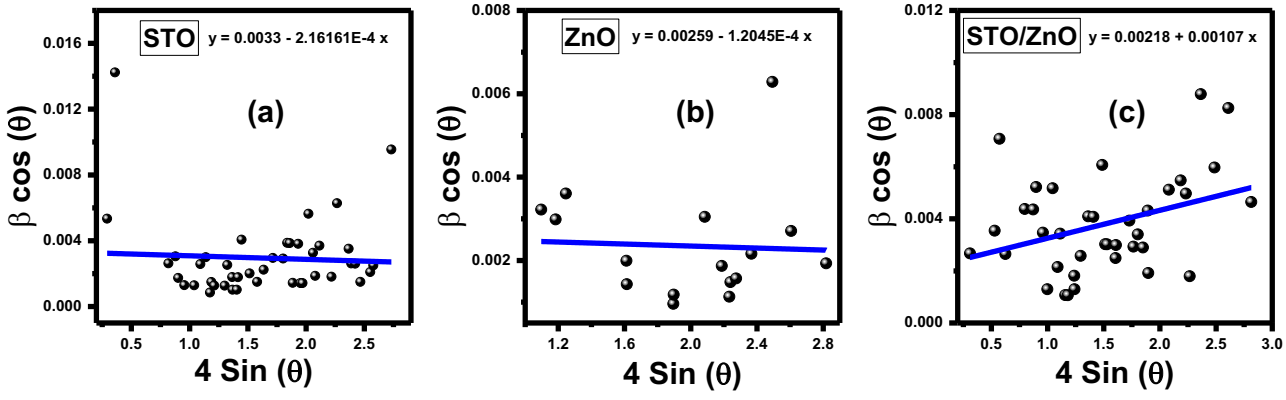

Figure 2: W–H plots of the investigated (a) STO, (b) ZnO, and (c) STO/ZnO.

where $I(hkl)/I_0(hkl)$ is the relative peak intensity, and N is the number of displayed diffraction peaks. TC indicates the texture of an assertive plane. If TC is greater than 1, the preferred orientation of growth is devoted to. For STO, the (310) peak has the highest intensity with a TC of 6.4, while for ZnO, the (101) peak has the greatest intensity with a TC of 3.9. The highest TC values indicate that monoclinic STO and hexagonal ZnO grow completely along (310) and (101) orientations, respectively. From Table S1, the average δ is very low (~0.11×10^{-3} dis·nm^{-2}).

3.1.2 SEM studies

Figure 3 shows the SEM images of the fabricated STO, ZnO, and STO/ZnO nanoparticles. Figure 3(a) illustrates that the synthesized STO appeared as a small, agglomerated nanoparticle. These nanoparticles have spherical shapes with different sizes, as displayed in Figure 3(b). The range of nanoparticle size is 45.6–94.7 nm. For ZnO, Figure 3(c) shows a hierarchical structure that creates a flower-like morphology. The high magnification image of ZnO reveals porous nanoflake aggregations (Figure 3(d)). The thickness of the nanoflakes ranges from about 6.4–9.6 nm. The average diameter of the nanopores is 12 nm. The STO/ZnO photocomposite has two phases, porous nanosheets and spherical nanoparticles, as presented in Figure 3(e and f). Besides, the distributed ZnO nanoparticles on the STO nanosheets formed a good network, which are closely interlinked with each other and might favor charge transfer in the photodegradation process.

3.1.3 EDX

Typically, EDX technology is employed to identify the chemical composition and quantitative ratios of the constituents. EDX was performed on the produced nanoparticle at

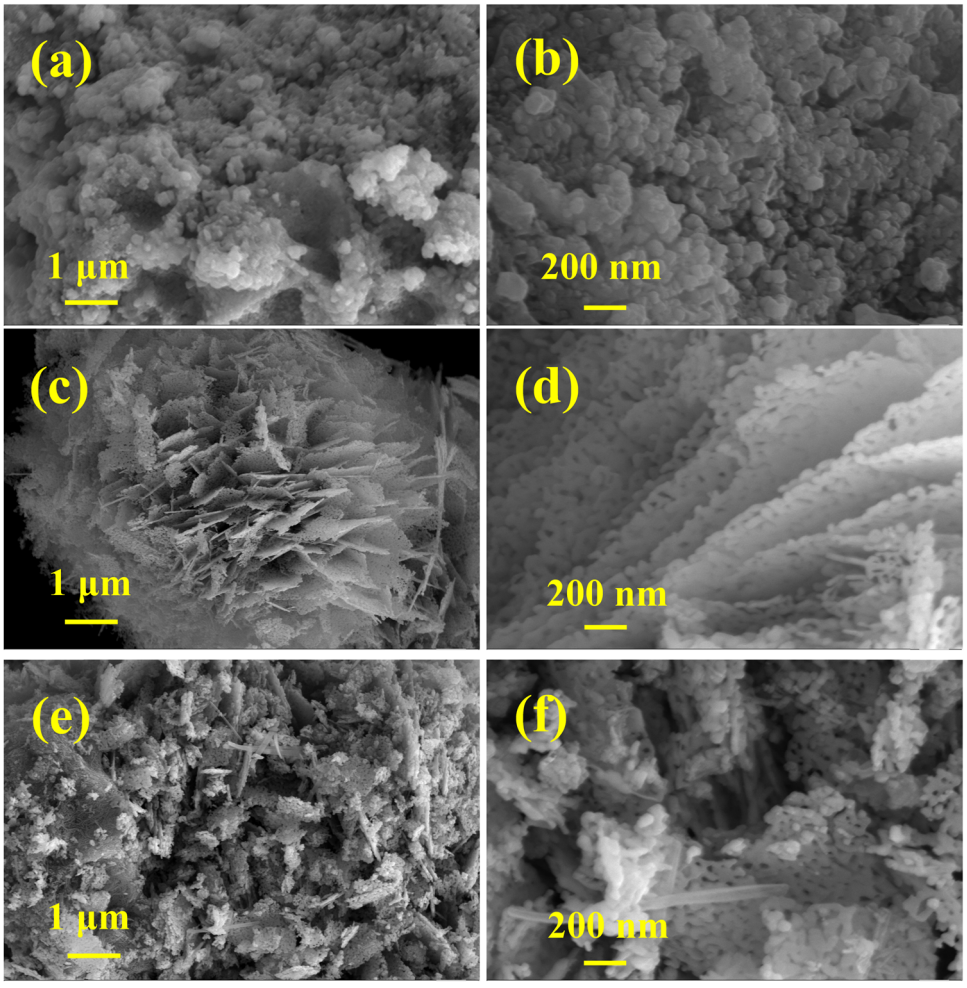

Figure 3: SEM images of the fabricated (a and b) STO, (c and d) ZnO, and (e and f) STO/ZnO at different magnifications.

a voltage of 15 kV. Figure S1 shows the EDX spectra for ZnO, STO, and STO/ZnO. For STO, there are only signals for Na, Ti, and O, as seen in Figure S1(a). Furthermore, no contaminants were detected in the EDX spectra, verifying the purity and crystallization of STO manufactured using an alkaline hydrothermal technique. As indicated in Figure S1(b), there are only signals for Zn and O. This demonstrates that the manufactured ZnO has great purity and good crystallization, which agrees with the XRD results. Figure S1(c) shows four signals for Na, Ti, Zn, and O, which confirm the formation of the STO/ZnO photocomposite.

3.1.4 Optical analysis

The optical behavior, absorption intensity, and energy gap properties of the photocomposite directly impact the efficiency of dye degradation. Figure 4 demonstrates the absorbance spectra of STO, ZnO, and mixed STO/*x*ZnO. The STO nanoparticles exhibited absorption onset at 270 nm and of ZnO at 360 nm. The valence band (VB) of this STO was formed by O 2p orbitals, while the conduction band (CB) was constituted by Ti 3d orbitals [32], [35]. The significant absorption band in the UV region of ZnO is due to the transfer of electrons from the VB to the CB of ZnO (O 2p → Zn 3d) [28]. The absorbance of all nanoparticles decreases with increasing wavelength in the visible region. The absorption edge of STO/*x*ZnO is shifted blue toward the visible region due to the modification of the electronic structure of STO/*x*ZnO. The width of the absorption band of these nanoparticles is large in the UV range. The STO/ZnO photocomposite has the highest light absorption intensity in the UV and visible regions. In other words, STO/ZnO absorbs more photons than other nanoparticles, which is better for producing electron–hole pairs and improving photocatalytic activity [54].

Materials that are amorphous, poorly crystalline, and disordered exhibit an absorption tail in the absorption spectrum. The Urbach energy (E_u) is related to this

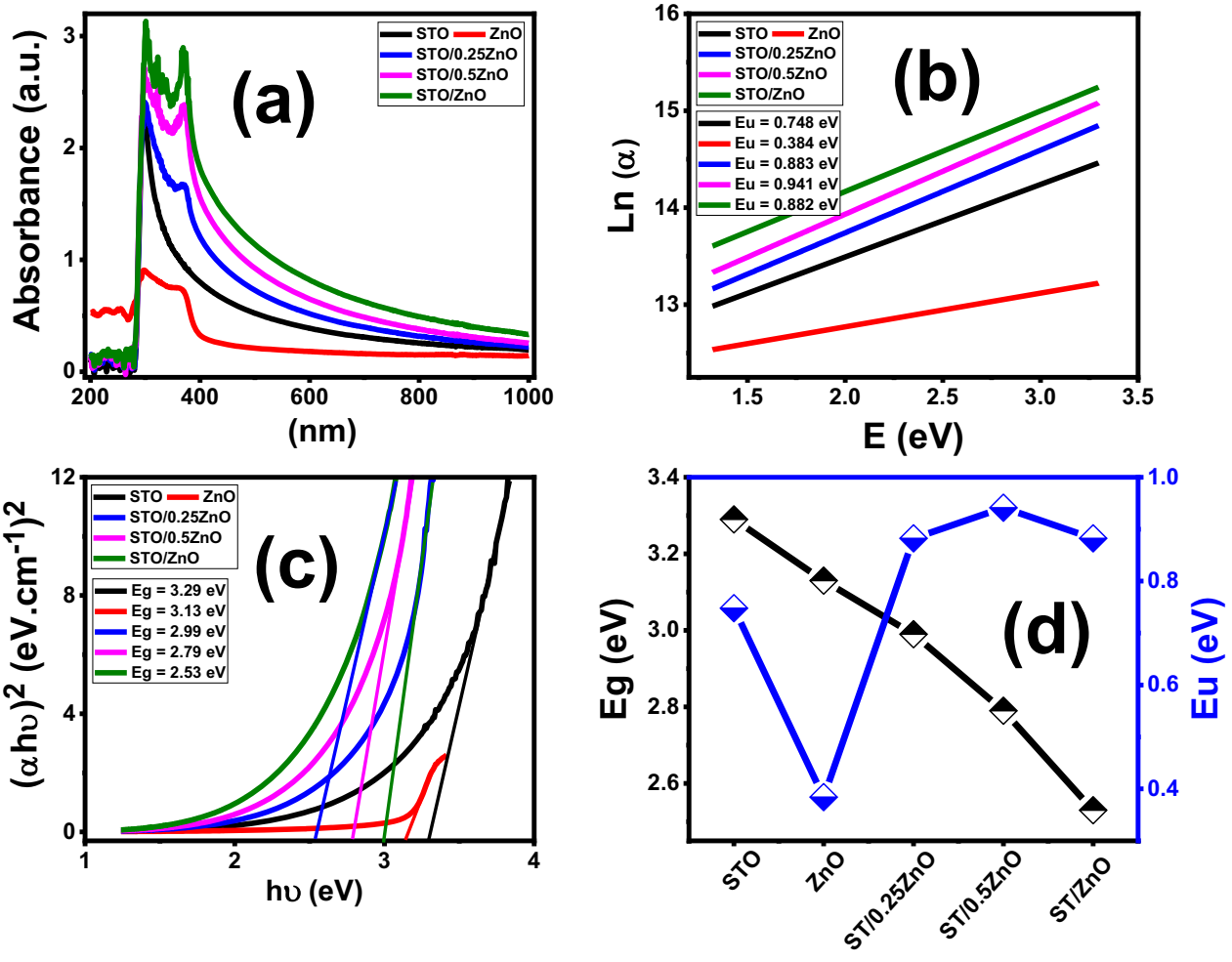

Figure 4: (a) Absorbance spectra (b), Tauc plot (c), Urbach energy, and (d) the values of E_g and E_u of all fabricated STO/*x*ZnO nanoparticles.

absorption tail, which is known as an Urbach tail. It is attributed to the materials having defect-localized states, which extended into the forbidden gap and led to the tail in the VB and CB [55,56]. The absorption coefficient spectrum gradually increases with increasing photon energy in a certain energy range due to the Urbach tail. E_u is defined by an exponential increase in the absorption coefficient with energy according to the following relationship [57]:

$$\alpha = \alpha_0 e^{E/E_u} \quad (5)$$

where α_0 and E_u are a constant and the Urbach energy, respectively. E_u can be derived from the slope of the fitting straight line of ln(α) versus the incident energy ($h\nu$), as shown in Figure 4(b). The E_u of ZnO is about 384 meV, which agrees with a previous work [58]. An increase in the width of the Urbach tail with ZnO weight can be observed. The values of the E_u increases from 747 to 881 meV for STO and STO/ZnO, respectively. The highest E_u of 941 meV is obtained for the STO/0.5ZnO.

The Kubelka–Munk and Tauc models were used to calculate the bandgap energies of the nanoparticles (Supplementary data). The E_g values of STO and ZnO were found to be 3.29 and 3.13 eV, respectively, as shown in Figure 4(c and d). This indicates that both STO and ZnO are suitable for photocatalysis applications under UV irradiation. When ZnO is combined with STO, the O 2p orbitals of ZnO are mixed with the O 2p orbitals of the STO, resulting in the creation of interband states, which lower the value of E_g. The solar spectrum consists of approximately 5% UV light, 45% visible light, and 50% near-infrared light. To achieve efficient light harvesting, it is crucial to adjust the bandgap of photocomposites towards the visible range. The photon energy in the visible region ranges from 1.5 to 2.5 eV. A narrow bandgap facilitates the easy transition of electrons from the VB to the CB when exposed to solar energy. The bandgap energies of STO/0.25ZnO, STO/0.5ZnO, and STO/ZnO are measured as 2.99, 2.79, and 2.53 eV, respectively. Consequently, the STO/ZnO photocomposite is considered the most suitable for photocatalytic applications.

3.1.5 BET analysis

The physical and chemical properties of the catalysts can be characterized by their textural properties, which include the surface area, pore volume, and mean pore diameter. The BET technique is commonly used to determine the surface area of porous materials. By employing the Barrett–Joyner–Halenda porosity model, the average pore size can be derived from the adsorption/desorption data. Measuring the physisorption of an inert gas, such as nitrogen, is a fundamental technique used to characterize the textural properties of porous nanoparticles. Nitrogen gas can penetrate the particles, pores, cracks, and surface irregularities of the nanoparticle due to its small molecular size. Through weak van der Waals forces, small gas molecules adhere to the solid nanoparticle and its porous structures, forming an adsorbed gas layer. The rate of adsorption allows for the calculation of the specific surface area and the porous geometry of the solid nanoparticle.

Figure 5 illustrates the nitrogen adsorption and desorption isotherm curves of three photocomposites: STO, ZnO, and STO/ZnO. The measured BET surface areas for STO, ZnO, and STO/ZnO are 14.1, 19.5, and 24.8 $m^2 \cdot g^{-1}$, respectively. The incorporation of STO with ZnO in the photocomposites significantly increases the surface area compared to the individual materials. Additionally, the STO/ZnO photocomposite exhibits a pore volume of 0.0653 $cm^3 \cdot g^{-1}$ and a mean pore diameter of 10.52 nm, surpassing the values of STO and ZnO. These results highlight the potential of STO/ZnO as a photocomposite for various applications, emphasizing its improved textural properties.

3.2 Photocatalytic measurements

3.2.1 Optimized the photocatalytic activity of STO/*x*ZnO nanoparticles

This section examines the photocatalytic activity of STO, ZnO, and STO/*x*ZnO nanoparticles using the MB dye degradation under 400-W tungsten lamp illumination and solar light irradiation. The photocomposite (50 mg) was added to

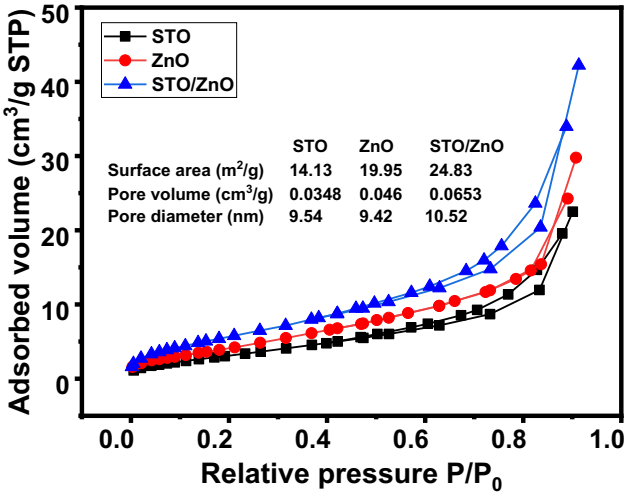

Figure 5: Nitrogen adsorption–desorption isotherms of STO, ZnO, and STO/ZnO nanoparticles.

an aqueous solution of MB (5 ppm, 50 mL) in a glass reactor. The reaction takes place in an air atmosphere at 25°C at pH = 7. The time-dependent absorption spectra of MB solutions were utilized to observe the concentration of MB. The absorption ranges from 600 to 700 nm with a high-intensity absorption peak at 664 nm.

Figure 6(a–f) shows the MB absorbance decay with time for photocatalytic reactions using different nanoparticles under tungsten lamp irradiation. The tungsten lamp, also known as the tungsten halogen lamp, is a good light source because it emits broadband spectral radiation from the long-wave UV through the visible and into the infrared wavelength regions [57]. Its emission spectrum ranges from 340 to 2,200 nm, which is similar to that of a blackbody emitter. The maximum peak intensity from a tungsten lamp is located near 1,000 nm, while it emits a very low intensity of radiation in the UV region below 400 nm. A control experiment of dye photolysis without a present catalyst by the light was carried out to effectively evidence the role of the photocomposite. There is little decrease in the absorption for the control test, which represents a very limited effect of the self-photodegradation rate of MB. After 60 min of tungsten lamp exposure, the absorption of MB solution decreases from an initial value of 1.2 to 0.86 and 0.92 in the presence of the STO and ZnO nanoparticles, respectively. These low results reflect visible light cannot induce electron transition in the STO and ZnO. For different STO/*x*ZnO photocomposites, the intensity of the absorption peak of MB solution in the presence of the STO/ZnO decreased rapidly higher than STO/0.25ZnO and STO/0.50ZnO with increasing irradiation time, as shown in Figure 6(d–f).

Under sunlight irradiation, the absorption of MB solution exhibits a very rapid decrease, as shown in Figure 7(a–f). The absorption of the MB solution of the STO/ZnO photocomposite decreases from 1.2 to 0.01 after 60 min. This indicates the STO/ZnO has the best catalytic activity under sunlight.

3.2.2 Photodegradation efficiency (PE%)

The percentage of PE% was calculated at λ = 664 nm using the following equation:

$$\mathrm{PE}(\%) = (1 - A_t/A_0) \times 100 \tag{6}$$

where A_0 represents the initial absorption of the MB dye solution at t = 0 s and A_t represents the final absorption of the MB dye at specified time intervals. Figure 8 displays the degradation efficiency of all prepared nanoparticles. Generally, degradation efficiency under sunlight irradiation is higher than under tungsten lamp irradiation at the same Illumination interval time. This is due to the emitted intensity from the tungsten lamp being centered at a wavelength of 1,000 nm.

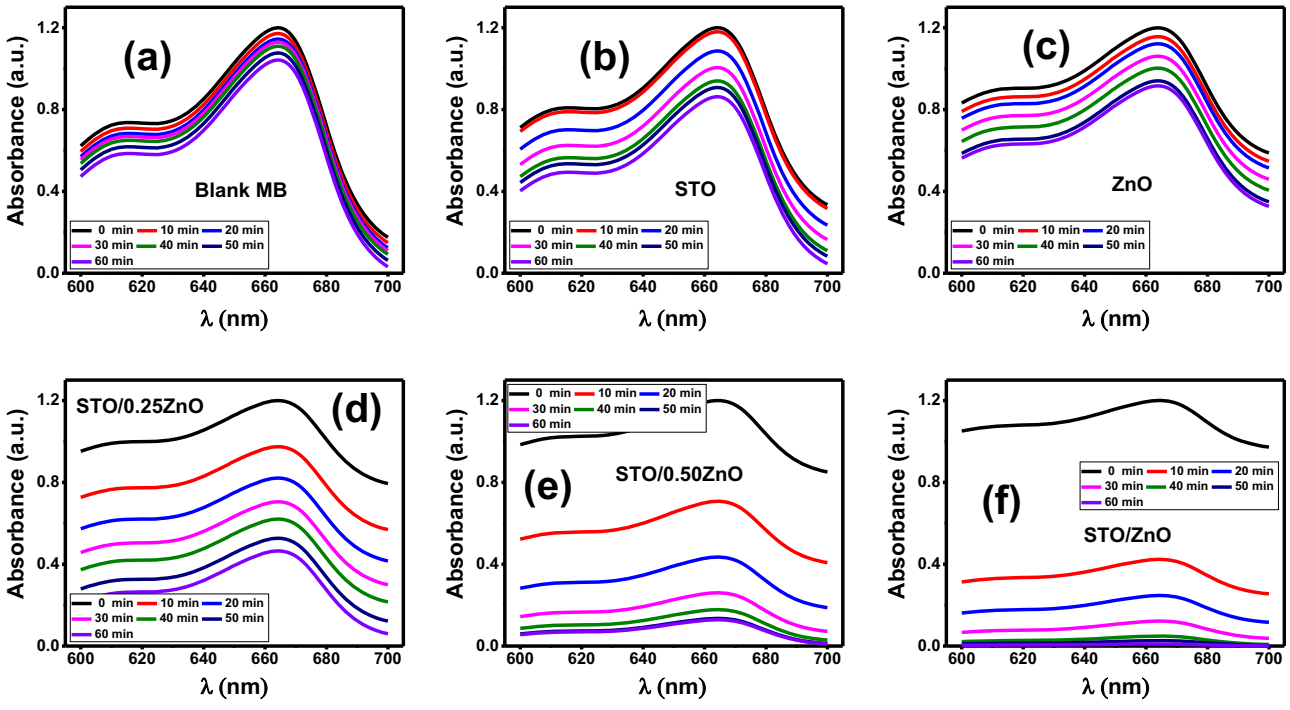

Figure 6: Spectra absorbance under tungsten lamp irradiation of a 5 ppm MB (50 mL) dye solution in the presence of 50 mg of photocomposites: (a) blank MB, (b) STO, (c) ZnO, (d) STO/0.25ZnO, (e) STO/0.50ZnO, and (f) STO/ZnO.

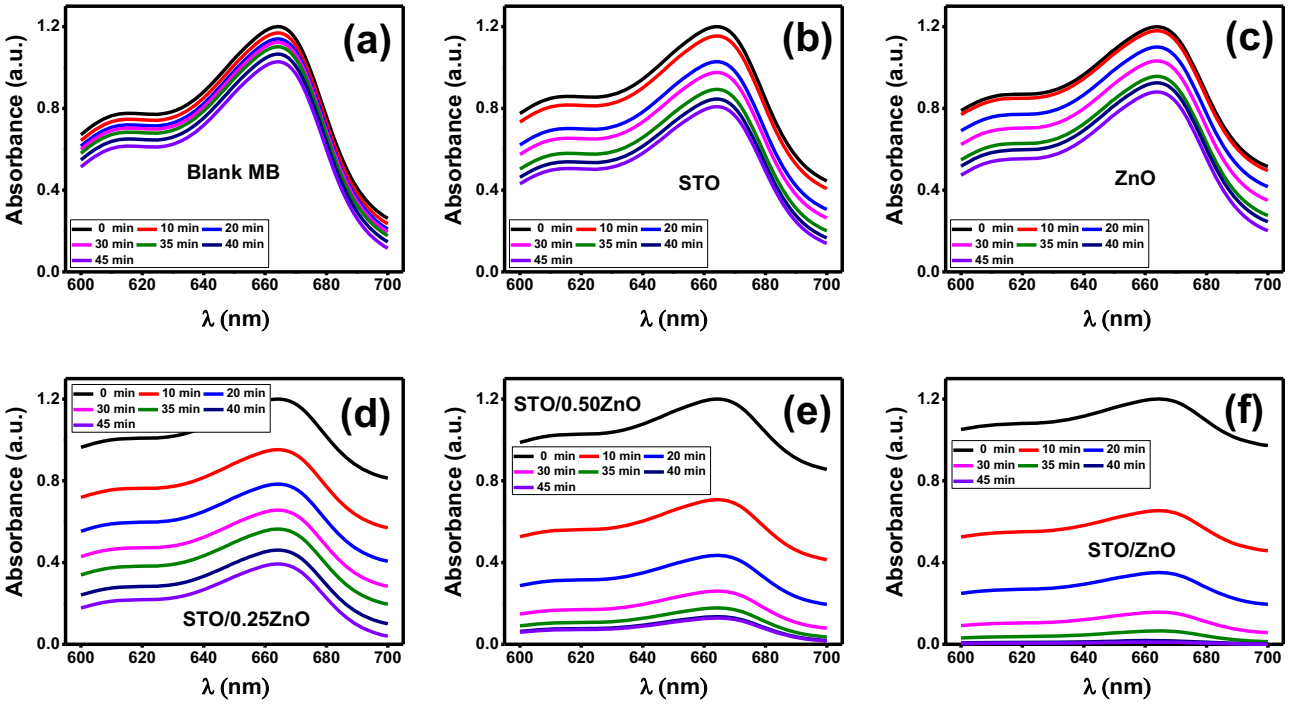

Figure 7: Spectra absorbance of a 5 ppm MB dye (50 mL) solution under sunlight irradiation in the presence of 50 mg of photocomposites: (a) blank, (b) STO, (c) ZnO, (d) STO/0.25ZnO, (e) STO/0.50ZnO, and (f) STO/ZnO.

Figure 8 shows that the photocatalytic degradation of the MB dye demonstrates an increase in the PE of the dye as illumination time increases for all nanoparticles. Also, the MB self-decomposition is limited. It is below 20% under sunlight and tungsten lamp illumination after 60 min. The degradation efficiency of both STO and ZnO after 60 min under natural sunlight and tungsten lamp is below 40%, Figure 8(a and b). The poor photocatalytic activity of STO and ZnO because of their high E_g.

The ZnO wt% ratio has a significant effect when comparing the photocatalytic activity process with only STO, as shown in Figure 8. The coupling between STO and ZnO

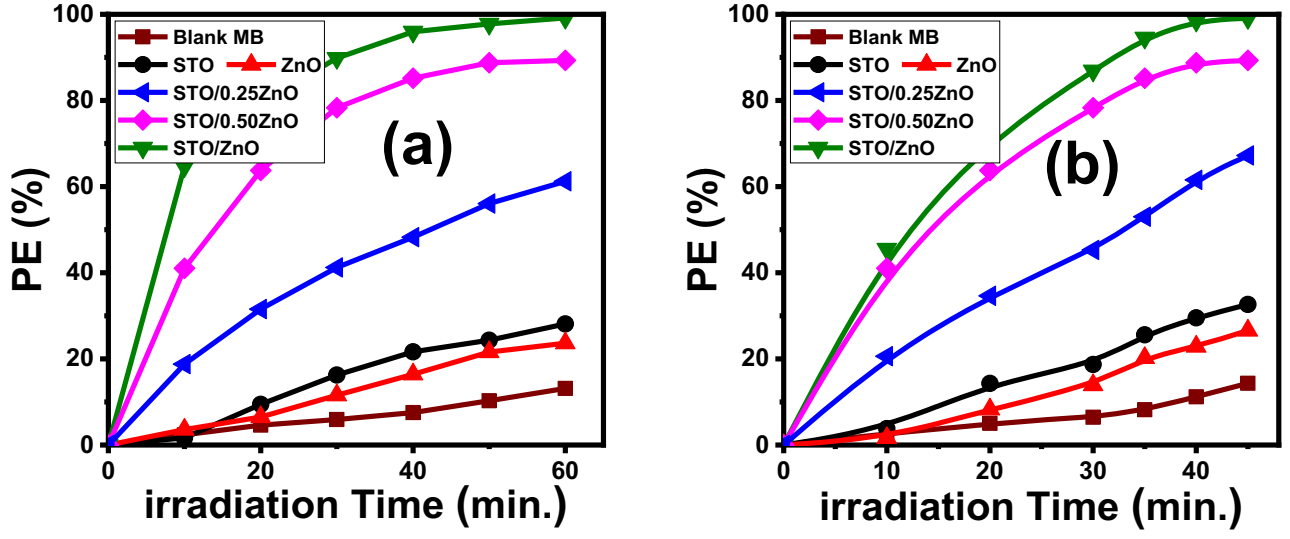

Figure 8: The PE% of 5 ppm MB dye solution (50 mL) using 50 mg of the prepared nanoparticles under (a) tungsten lamp irradiation and (b) solar light irradiation.

exhibited superior photocatalytic behavior. The photocatalytic activity increases by increasing the ZnO content in the STO/*x*ZnO photocomposite. The efficiency of STO/0.25ZnO and STO/0.5ZnO is 67% and 89% under sunlight, respectively. The STO/ZnO photocomposite exhibits the best photocatalytic activity. It reached complete photocatalytic degradation (~100%) after 60 min, as shown in Figure 8(b) under solar light. The results indicated that the photocatalytic efficiency for STO/ZnO was about four times that of the bare STO and ZnO.

The enhanced photocatalytic performance of the STO/ZnO photocomposite can be attributed to multiple factors. First, STO/ZnO demonstrates the highest light absorption capability compared to other photocomposites. Second, it possesses a narrow bandgap (E_g), which leads to increased generation of electron–hole pairs when irradiated with visible light. Third, the unique interlinked structure of STO/ZnO facilitates the movement of reactant and product molecules, promoting easier chemical reactions. Fourth, the distribution of ZnO over the STO structure results in a higher surface area, accelerating the generation of reaction oxidizing species. The synergistic effect between STO and ZnO enables efficient charge transfer. Additionally, the formation of a p–n junction between STO and ZnO nanoparticles modifies the electronic states and band alignment, creating a built-in electric field across the junction. This electric field plays a crucial role in preventing carrier recombination and extending the lifetime of electron–hole pairs [40], [48,59]. Taken together, these combined factors contribute to the superior catalytic performance of STO/ZnO. Nezamzadeh-Ejhieh and Karimi-Shamsabadi substantiated the generation of chloride, nitrate, and sulfate anions as intermediates in the degradation process of MB solution [60].

To verify whether STO/ZnO qualifies as a photocomposite rather than a mere physical mixture, an additional photodegradation experiment was conducted. In this experiment, STO nanoparticles and ZnO nanoparticles were initially physically mixed and employed for the photodecomposition of MB under natural sunlight. A notable distinction in the efficiency of dye removal was observed between the STO/ZnO photocomposite and the mixture of STO and ZnO particles, as shown in Figure S3 (Supplementary data). The results demonstrated that the STO/ZnO photocomposite exhibited superior photocatalytic performance compared to the mixture of STO and ZnO particles. This discrepancy strongly suggests the presence of p–n-type junctions within the STO/ZnO photocomposite. Furthermore, the integration of STO and ZnO at the nanoscale generated synergistic effects that significantly enhanced the photocatalytic properties of the STO/ZnO photocomposite. Based on these findings, it can be confidently concluded that the STO/ZnO material is indeed a photocomposite rather than a mere physical mixture.

3.2.3 TOC analysis and biocompatibility experimental

To assess the mineralization of MB through the catalytic activity process, the concentration of TOC was investigated. The TOC serves as a crucial parameter for measuring the amount of organic contamination in water. The TOC determination process involved mixing the dye solution with phosphoric acid, sodium persulfate, and potassium hydrogen phthalate. Figure 9 represents the TOC levels during the photocatalytic degradation of MB using different photocomposites. The results demonstrate reductions in TOC values of 2.33, 1.33, and 0.37 when STO, ZnO, and STO/ZnO were, respectively, employed as photocomposites. Higher TOC levels indicate water with a more substantial amount of organic contamination. It is noteworthy that the STO/ZnO catalyst exhibited the highest degree of mineralization for MB, indicating its effectiveness in converting MB into CO_2 and H_2O.

To assess biocompatibility, experiments were conducted to evaluate the growth and productivity of plants [61]. In this experiment, fenugreek seeds were cultivated using both the untreated dye solution and the solution obtained after the photodegradation process. Figure S4 provides visual evidence, illustrating the distinct impact of the two solutions on seed growth. The results showed that fenugreek seeds watered with the untreated solution exhibited poor growth. In contrast, the seeds cultivated in the photocatalytically treated solution displayed significant development and rapid growth. These findings suggest that the treated solution is biocompatible with fenugreek seeds and holds great promise for agricultural applications.

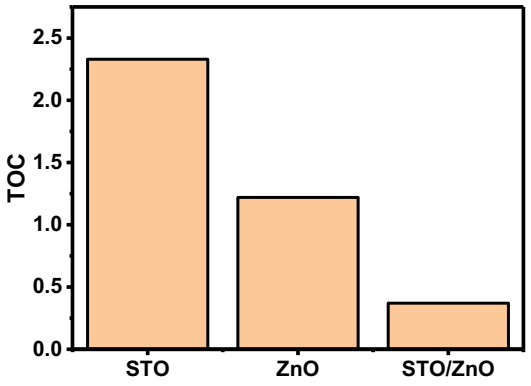

Figure 9: TOC analysis of 5 ppm MB dye solution (50 mL) using 50 mg of the prepared STO, ZnO, and STO/ZnO nanoparticles.

3.2.4 Effect of STO/ZnO dosage and MB concentration

The MB photocatalytic activity using different quantities of STO/ZnO is exemplified graphically in Figure 10(a and b). The photo-reactions of MB were studied at an MB concentration of 5 ppm for 60 min under continuous solar light exposure. The catalyst dose increases from 10 to 50 mg. Higher dosages of STO/ZnO has strong positive impact in enhancing its photodegradation performance for MB. The dye DE increases from 70.5% to 100% with increasing STO/ZnO from 10 to 50 mg, as shown in Figure 10(b). The aforementioned improvement is linked to the associated increase in surface area, adsorbed capacity, available catalytic sites, and formed active oxidizing species [62]. Besides, the increase in the photogenerated hydroxyl radical groups and the positive holes increase with the catalyst mass.

The performance of STO/ZnO in the photodegradation of higher concentrations of MB from 5 to 100 ppm was studied using 50 mg of the nanoparticle as the applied catalyst quantity mass. The photocatalytic activity of STO/ZnO decreases with high MB concentrations, as displayed in Figure 10(c and d). This effect is related to adsorbed MB molecules on the surface of STO/ZnO in blocking its active site [63]. Also, high concentrations of MB can cause light scattering, which in turn obstructs the interaction between incident light and the surface of STO/ZnO in the solution. This leads to a reduction in the formation of photogenerated carriers. As a consequence, there is a decrease in the degradation percentage as the initial dye concentration increases [64].

3.2.5 Kinetic models and photodegradation rate constants

The photodegradation rate constant (k) of the STO/xZnO nanoparticles for MB degradation under sunlight illumination was calculated based on many kinetic models. The

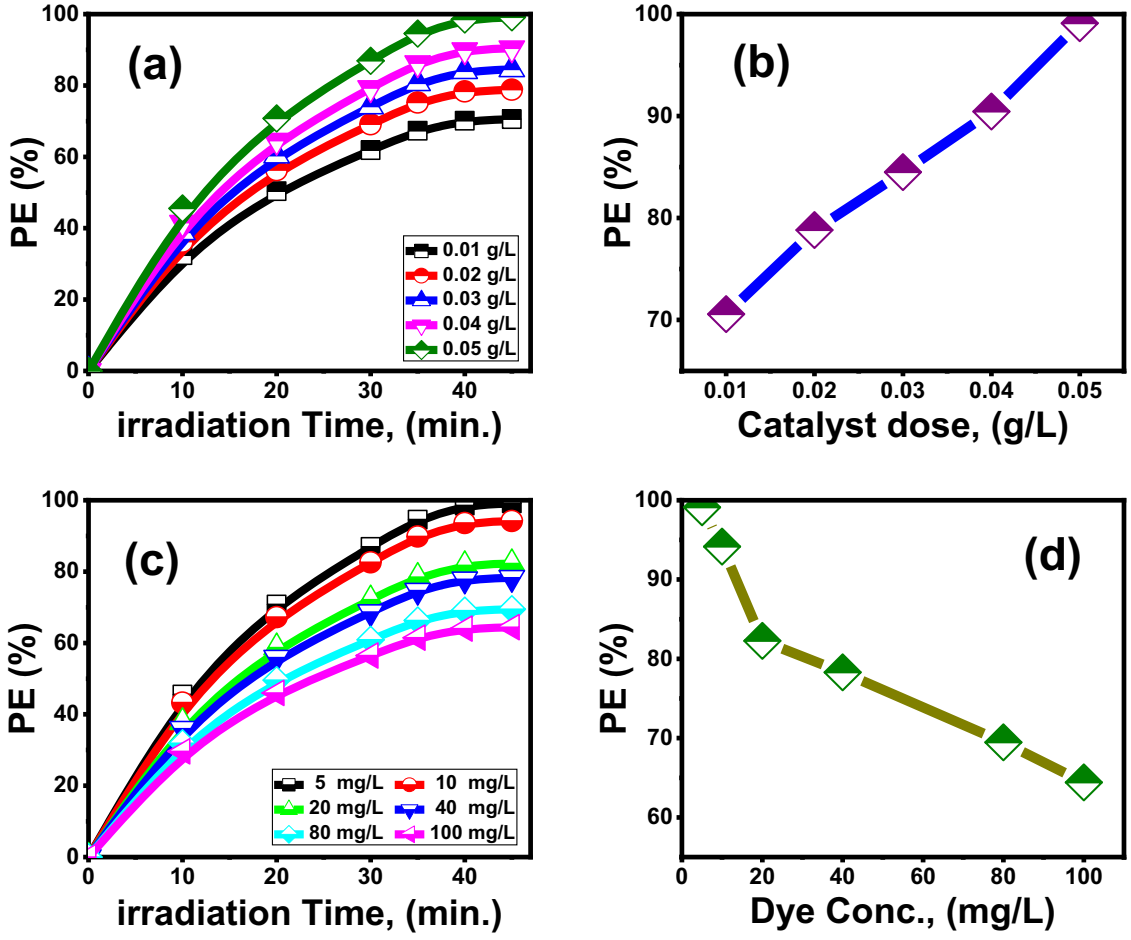

Figure 10: Influence of the main factors on the degradation of MB using STO/ZnO as a photocomposite under sunlight. (a and b) Effect of the photocomposite dose on photodegradation for STO/ZnO, and (c and d) effect of the initial dye concentration on the photodegradation for STO/ZnO.

kinetic models investigated are the zero-, first-, and second-order (n = 0, 1, 2) models, which can be expressed by the following equations:

$$C_t = -k_0 t + C_0 \quad (7)$$

$$\ln(C_0/C_t) = k_1 t \quad (8)$$

$$1/C_t = k_2 t + 1/C_0 \quad (9)$$

where C_0 and C_t are the MB concentrations at the initial reaction and reaction time (t), respectively. The linear relations of zero, first, and second orders were estimated through linear regression plotting of C_t, $\ln(C_0/C_t)$, and $1/C_t$ against time, respectively, as shown in Figure 11. The slopes

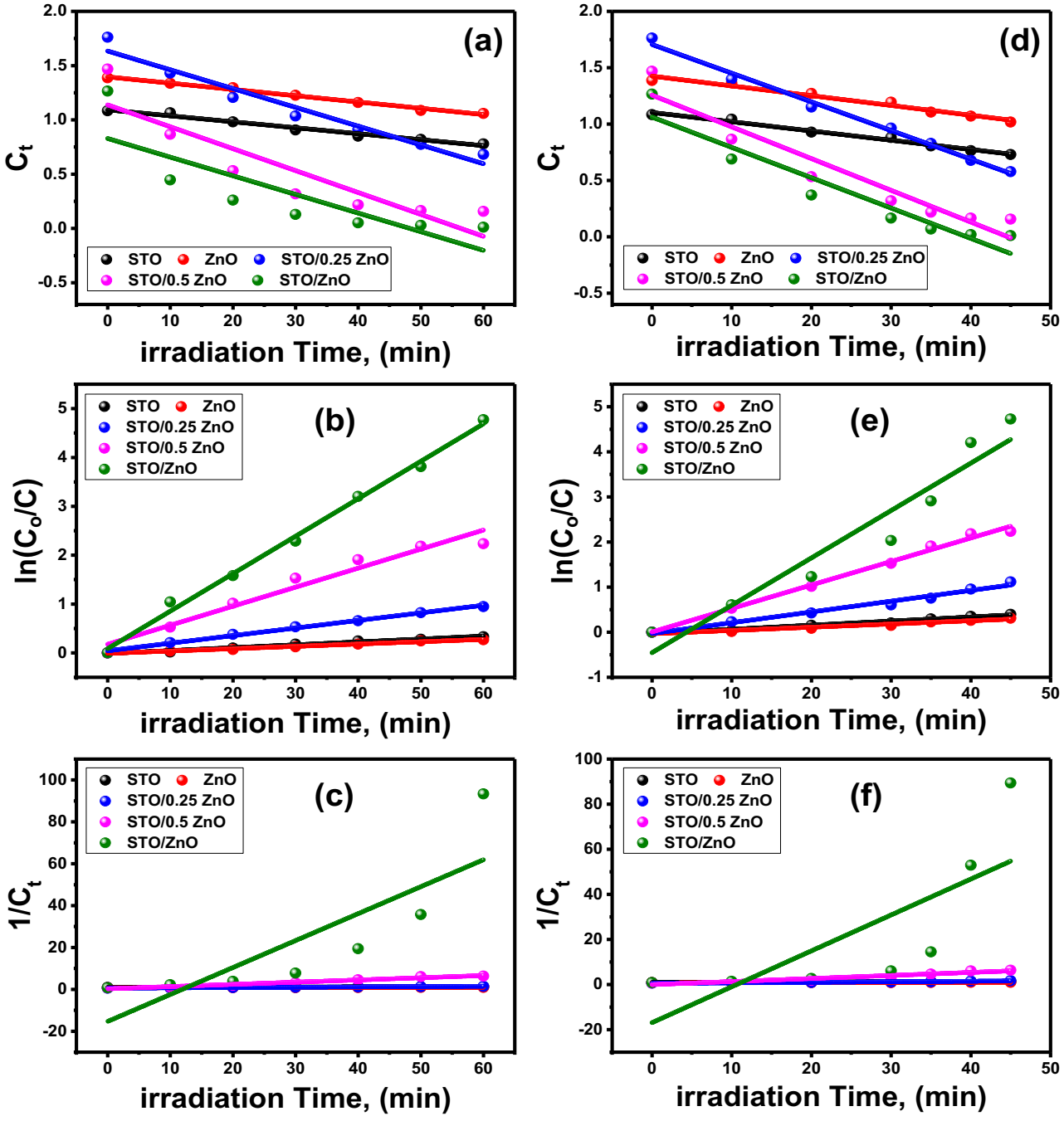

Figure 11: Fitting of the photodegradation data of 5 ppm MB dye using the STO/xZnO nanoparticles with (a) zero order, (b) first order, and (c) second order under tungsten lamp illumination and using STO/xZnO nanoparticles with (d) zero order, (e) first order, and (f) second order under sunlight illumination.

of the straight lines represent the k. The high values of the correlation coefficient (R^2) indicated a good degree of fitting the data with the kinetic model. The kinetic parameters related to models, including fitting equation, the values of k, and R^2 are presented in Table S2. For STO/xZnO, the values of $k_2 > k_1 > k_0$ for the same nanoparticle under sunlight. Also, k for all models gradually increases with increasing the weight ratio of ZnO content. The STO/ZnO photocomposite has a high value of k_2 = 1.592 min^{-1} and very poor fitting R^2 = 0.0.502. The values of the theoretical kinetic rate constants of the STO/ZnO photocomposite under sunlight agree with the estimated experimental results in Figure 8. The STO/ZnO photocomposite has the highest correlation coefficient value (R^2 = 0.995) for the first-order model. Hence, the photodegradation of MB is better represented by the first-order model.

3.2.6 Recyclability studies

Recyclability is one of the most essential aspects of practical applications. It measures the possibility of reusing the photocomposite numerous times for dye degradation. The recyclability depends on the photostability of the photocomposite during reactions. The reusability of the STO/ZnO for several runs of MB dye photodegradation was studied using a 5 ppm MB dye solution, as shown in Figure 12. The photocatalytic reaction was performed under the closely same conditions, ensuring nearly consistent levels of sunlight intensity and temperature for all experimental runs. Following each test, the STO/ZnO solid fractions were rinsed with DW, dried at 70°C for 10 h, and then utilized once again in the subsequent test. The PE for the first run is 100% in 60 min.

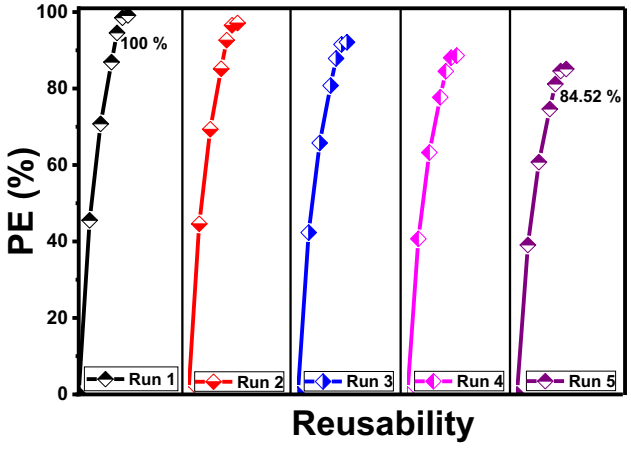

Figure 12: Reusability of the optimum STO/ZnO photocomposite for the photodegradation of 5 ppm MB (50 mL) dye solution using 50 mg of catalyst for five cycles.

Then, the PE decreases to 84.52% after five runs (Figure 12). The observed decrease in dye PE from the first to the fifth runs could indeed be influenced by various factors. One possibility is the binding of photoreaction by-products on the surface of the STO/ZnO catalyst. This can lead to the blockage of active sites and a decrease in photocatalytic activity, resulting in a lower efficiency. In addition to the possible leaching of the STO/ZnO photocomposite under the extensive washing procedure, this could lead to a reduction in the mass of the catalyst per unit volume of the dye solution, which may contribute to the decrease in PE. This indicates that the material is effective in removing dye and exhibits high stability.

3.2.7 EIS

EIS was used to evaluate electron/hole separation efficiencies for STO, ZnO, and STO/ZnO. Frequency analysis was conducted from 10 mHz to 100 kHz, 0 V at room temperature (25°C). The resulting Nyquist plots are shown in Figure 13. The y-axis represents the imaginary part of impedance (Z_i), while the x-axis represents the real part (Z_r). The observed curve consisted of a half-semicircle and a straight line for all nanoparticles. An equivalent Randles circuit was employed to model electrical behavior, and the circuit parameters are listed in Table S3. The calculated resistance for the ZnO/STO photocomposite was 10,931 kΩ, which is lower than that for ZnO (12,216 kΩ) and STO (31,788 kΩ), indicating improved charge transport. Admittance measures the ease of current flow. The admittance values (Y) for ZnO, STO, and ZnO/STO were 21,694, 15,274, and 47,342 μS, respectively. These results suggest favorable charge transfer kinetics for the ZnO/STO photocomposite, which is beneficial for photodegradation reactions. Hence, EIS analysis demonstrated a significant reduction in charge recombination, indicating improved electron/hole separation efficiencies for the ZnO/STO photocomposite [65].

3.2.8 Mechanism of photodegradation

The proposed mechanism for STO/ZnO photocatalysis relies on the absorption of photons, which excite electrons from the VB to the CB, creating electron–hole pairs [66,67]. However, in individual STO and ZnO, these electron–hole pairs tend to recombine, diminishing their effectiveness in the photocatalytic process. To overcome this limitation, the STO/ZnO composite incorporates a potential barrier at their interface [48,59]. This barrier arises from the interaction between the p-type STO and n-type ZnO semiconductors, generating internal electric fields and causing adjustments

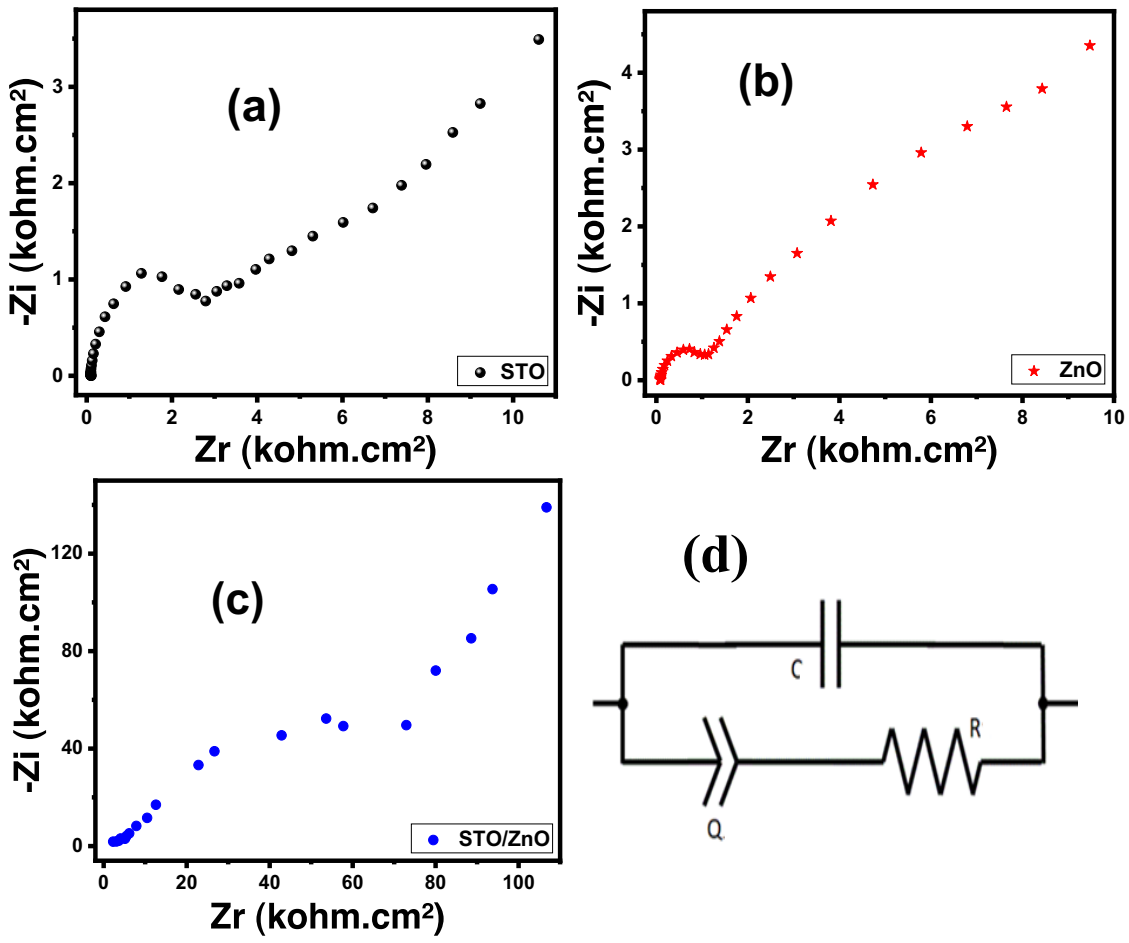

Figure 13: Nyquist plot of EIS of all nanoparticles (a) STO, (b) ZnO, (c) STO/ZnO, and (d) the equivalent Randles circuit.

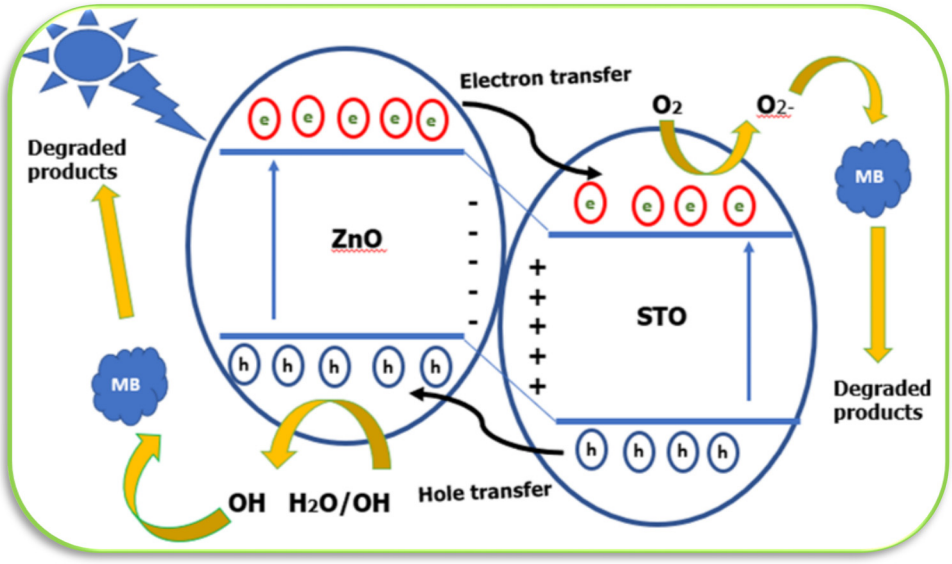

Figure 14: Schematic diagram for the formation of an energy band diagram of a p–n junction and charge transfer in an STO/ZnO-based photo-composite under visible light illumination.

in the energy band alignment, as illustrated in Figure 14. These adjustments continue until the Fermi level reaches a new equilibrium. Consequently, electrons migrate from the CB of ZnO to the CB of STO, driven by the energy gradient resulting from the differing CB levels of the two materials [68]. This electron transfer leads to an accumulation of electrons in STO, while holes move from the VB of STO to the VB of ZnO, accumulating in ZnO. The potential barrier acts as a physical impediment, restraining the movement of charge carriers and compelling the photogenerated electrons and holes to remain confined within their respective regions for an extended duration. By maintaining this prolonged separation of charge carriers within STO and ZnO, they can actively engage in their respective redox reactions.

During photocatalysis, the MB is excited from the ground state to the excited state (MB*) when exposed to sunlight. The positive holes (h^+) can react with water molecules (H_2O) or hydroxide ions (OH^-) to produce highly reactive hydroxyl radicals ($OH^{\cdot}$) [69]. Simultaneously, the negative electrons (e^-) are captured by adsorbed oxygen molecules (O_2), resulting in the formation of superoxide anion radicals ($O_2^{\cdot-}$). These reactive species are primarily responsible for attacking and breaking down the adsorbed MB dye molecules on the surface of the p-STO/n-ZnO photocomposite. The oxidizing radicals can ultimately transform the MB molecules into water (H_2O) and carbon dioxide (CO_2). The following equations provide a summary of the mechanism of MB dye degradation over the STO/ZnO photocomposite [70,71]:

$$\text{STO/ZnO} + h\nu \rightarrow \text{STO/ZnO}(e^-_{CB} + h^+_{VB}) \quad (10)$$

$$\text{MB dye} + h\nu \rightarrow \text{MB*dye}(e^-_{CB} + h^+_{VB}) \quad (11)$$

$$h^+ + H_2O \rightarrow OH^{\cdot} + H^+ \quad (12)$$

$$h^+ + OH^- \rightarrow OH^{\cdot} \quad (13)$$

$$e^- + O_2 \rightarrow O_2^{\cdot-} \quad (14)$$

$$OH^{\cdot}, O_2^{\cdot-} + \text{MB dye}(h^+_{VB}) \rightarrow \text{products}(CO_2 + H_2O) \quad (15)$$

$$h^+ + \text{MB dye} \rightarrow \text{product}(CO_2 + H_2O) \quad (16)$$

4 Conclusions

The low-cost hydrothermal method was utilized to synthesize a range of nanoparticles, including STO, ZnO, STO/0.25ZnO, STO/0.5ZnO, and STO/ZnO. By optimizing the weight ratios of ZnO, the highest PE was achieved with the STO/ZnO photocomposite. After 1 h of solar irradiation, the degradation percentages of MB were measured as 33.7% for STO, 25.8% for ZnO, and an impressive 100% for STO/ZnO. Additionally, these photocomposites exhibited excellent stability and could be reused multiple times. The improved optical properties and the formation of a PN junction contributed to the enhanced photodegradation performance of STO/ZnO. Consequently, the STO/ZnO photocomposite is suitable and efficient in wastewater purification.

Acknowledgments: This work was supported and funded by the Deanship of Scientific Research at Imam Mohammad Ibn Saud Islamic University (IMSIU) (grant number IMSIU-RG23130).

Funding information: The research was funded by the Deanship of Scientific Research at Imam Mohammad Ibn Saud Islamic University (IMSIU) (grant number IMSIURG23130).

Author contributions: Mohamed Zayed and Amna Tarek: methodology, software, formal analysis, and writing – review & editing. Mervat Nasr: methodology, investigation, and software. Ashour M. Ahmed and Mamduh J. Aljaafreh: conceptualization, formal analysis, and writing – review & editing. Mohammad Marashdeh and M. Al-Hmoud: validation, investigation, formal analysis. Mohamed Rabia and Mohamed Shaban: data curation, validation, and resources.

Conflict of interest: Authors state no conflict of interest.

Data availability statement: The datasets generated during and/or analyzed during the current study are available from the corresponding author on reasonable request.

References

[1] Rehman MSU, Munir M, Ashfaq M, Rashid N, Nazar MF, Danish M, et al. Adsorption of Brilliant Green dye from aqueous solution onto red clay. Chem Eng J. Jul. 2013;228:54–62. doi: 10.1016/J.CEJ.2013.04.094.

[2] Drumond Chequer FM, de Oliveira G, Anastacio Ferraz ER, Carvalho J, Boldrin Zanoni MV, de Oliveir DP. Textile dyes: Dyeing process and environmental impact. Eco-Friendly Text Dye Finish. 2013;6(6):151–76. doi: 10.5772/53659.

[3] Li H, Cao X, Zhang C, Yu Q, Zhao Z, Niu X, et al. Enhanced adsorptive removal of anionic and cationic dyes from single or mixed dye solutions using MOF PCN-222. RSC Adv. Mar. 2017;7(27):16273–81. doi: 10.1039/C7RA01647F.

[4] Mittal H, Mishra SB. Gum ghatti and Fe3O4 magnetic nanoparticles based nanocomposites for the effective adsorption of rhodamine B. Carbohydr Polym. Jan. 2014;101(1):1255–64. doi: 10.1016/J.CARBPOL.2013.09.045.

[5] Moradi N, Jamshidi M, Ghamarpoor R, Moghbeli MR. Surface functionalization/silane modification of CeO2 nanoparticles and their influences on photocatalytic activity of acrylic films for methylene blue removal. Prog Org Coat. Oct. 2023;183:107787. doi: 10.1016/J.PORGCOAT.2023.107787.

[6] Din MI, Khalid R, Najeeb J, Hussain Z. Fundamentals and photocatalysis of methylene blue dye using various nanocatalytic

assemblies – a critical review. J Clean Prod. May 2021;298:126567. doi: 10.1016/J.JCLEPRO.2021.126567.
[7] Mekatel EH, Amokrane S, Aid A, Nibou D, Trari M. Adsorption of methyl orange on nanoparticles of a synthetic zeolite NaA/CuO. Comptes Rendus Chim. Mar. 2015;18(3):336–44. doi: 10.1016/J.CRCI.2014.09.009.
[8] Al-Tohamy R, Ali SS, Li F, Okasha KM, Mahmoud YA, Elsamahy T, et al. A critical review on the treatment of dye-containing wastewater: Ecotoxicological and health concerns of textile dyes and possible remediation approaches for environmental safety. Ecotoxicol Env Saf. Feb. 2022;231:113160. doi: 10.1016/J.ECOENV.2021.113160.
[9] Forgacs E, Cserháti T, Oros G. Removal of synthetic dyes from wastewaters: a review. Env Int. Sep. 2004;30(7):953–71. doi: 10.1016/J.ENVINT.2004.02.001.
[10] Dutta S, Gupta B, Srivastava SK, Gupta AK. Recent advances on the removal of dyes from wastewater using various adsorbents: a critical review. Mater Adv. Jul. 2021;2(14):4497–531. doi: 10.1039/D1MA00354B.
[11] Derikvandi H, Nezamzadeh-Ejhieh A. An effective wastewater treatment based on sunlight photodegradation by SnS2–ZnS/clinoptilolite composite. Solid State Sci. Mar. 2020;101:106127. doi: 10.1016/J.SOLIDSTATESCIENCES.2020.106127.
[12] Babich IV, Moulijn JA. Science and technology of novel processes for deep desulfurization of oil refinery streams: a review. Fuel. Apr. 2003;82(6):607–31. doi: 10.1016/S0016-2361(02)00324-1.
[13] Wang Q, Jin R, Yin C, Wang M, Wang J, Gao S. Photoelectrocatalytic removal of dye and Cr(VI) pollutants with Ag2S and Bi2S3 co-sensitized TiO2 nanotube arrays under solar irradiation. Sep Purif Technol. Jan. 2017;172:303–9. doi: 10.1016/J.SEPPUR.2016.08.028.
[14] Massey AT, Gusain R, Kumari S, Khatri OP. Hierarchical microspheres of MoS2 nanosheets: Efficient and regenerative adsorbent for removal of water-soluble dyes. Ind Eng Chem Res. Jul. 2016;55(26):7124–31. doi: 10.1021/ACS.IECR.6B01115.
[15] Ma J, Yu F, Zhou L, Jin L, Yang M, Luan J, et al. Enhanced adsorptive removal of methyl orange and methylene blue from aqueous solution by alkali-activated multiwalled carbon nanotubes. ACS Appl Mater Interfaces. Nov. 2012;4(11):5749–60. doi: 10.1021/AM301053M.
[16] Sui ZY, Cui Y, Zhu JH, Han BH. Preparation of Three-dimensional graphene oxide-polyethylenimine porous materials as dye and gas adsorbents. ACS Appl Mater Interfaces. Sep. 2013;5(18):9172–9. doi: 10.1021/AM402661T.
[17] Saothayanun TK, Sirinakorn TT, Ogawa M. Layered alkali titanates (A2TinO2n+1): possible uses for energy/environment issues. Front Energy. Sep. 2021;15(3):631–55. doi: 10.1007/S11708-021-0776-6.
[18] Shirpour M, Cabana J, Doeff M. New materials based on a layered sodium titanate for dual electrochemical Na and Li intercalation systems. Energy Env Sci. Jul. 2013;6(8):2538–47. doi: 10.1039/C3EE41037D.
[19] Zaki AH, Abdel Hafiez M, El Rouby WMA, El-Dek SI, Farghali AA. Novel magnetic standpoints in Na2Ti3O7 nanotubes. J Magn Magn Mater. Apr. 2019;476:207–12. doi: 10.1016/J.JMMM.2019.01.002.
[20] Liu W, Zhao X, Wang T, Fu J, Ni J. Selective and irreversible adsorption of mercury(II) from aqueous solution by a flower-like titanate nanomaterial. J Mater Chem A. Aug. 2015;3(34):17676–84. doi: 10.1039/C5TA04521E.
[21] Iani IM, Teodoro V, Marana NL, Coleto U, Sambrano JR, Simões AZ, et al. Cation-exchange mediated synthesis of hydrogen and sodium titanates heterojunction: Theoretical and experimental insights toward photocatalyic mechanism. Appl Surf Sci. 2021;538(July 2020):148137. doi: 10.1016/j.apsusc.2020.148137.
[22] Lei X, Li X, Ruan Z, Zhang T, Pan F, Li Q, et al. Adsorption-photocatalytic degradation of dye pollutant in water by graphite oxide grafted titanate nanotubes. J Mol Liq. 2018;266:122–31. doi: 10.1016/j.molliq.2018.06.053.
[23] Samir H, Taha M, El-Dek SI, Zaki AH. Electronic structures and electrical properties of Cr^{2+}-, Cu^{2+}-, Ni^{2+}-, and Zn^{2+}-doped sodium titanate nanotubes. ACS Omega. Aug. 2022;7(31):27587–27601. doi: 10.1021/ACSOMEGA.2C03170.
[24] Kumar S, Nepak D, Kansal SK, Elumalai S. Expeditious isomerization of glucose to fructose in aqueous media over sodium titanate nanotubes. RSC Adv. Aug. 2018;8(53):30106–14. doi: 10.1039/C8RA04353A.
[25] Leyet Y, Guerrero F, Anglada-Rivera J, de Souza R, Brito WR, Aguilera L, et al. Synthesis of Na2Ti3O7 nanoparticles by sonochemical method for solid state electrolyte applications. J Solid State Electrochem. May 2018;22(5):1315–9. doi: 10.1007/S10008-017-3697-X.
[26] Zaki AH, Naeim AA, EL-Dek SI. Sodium titanate nanotubes for efficient transesterification of oils into biodiesel. Env Sci Pollut Res. Dec. 2019;26(36):36388–400. doi: 10.1007/S11356-019-06602-Z.
[27] Zhang H, Gao XP, Li GR, Yan TY, Zhu HY. Electrochemical lithium storage of sodium titanate nanotubes and nanorods. Electrochim Acta. Oct. 2008;53(24):7061–8. doi: 10.1016/J.ELECTACTA.2008.05.036.
[28] Zayed M, Nasser N, Shaban M, Alshaikh H, Hamdy H, Ahmed AM. Effect of Morphology and Plasmonic on Au/ZnO Films for Efficient Photoelectrochemical Water Splitting. Nanomater. Sep. 2021;11(9):2338. doi: 10.3390/NANO11092338.
[29] Tsai CC, Teng H. Nanotube formation from a sodium titanate powder via low-temperature acid treatment. Langmuir. Apr. 2008;24(7):3434–8. doi: 10.1021/LA702839U.
[30] Becker I, Hofmann I, Müller FA. Preparation of bioactive sodium titanate ceramics. J Eur Ceram Soc. Jan. 2007;27(16):4547–53. doi: 10.1016/J.JEURCERAMSOC.2007.03.024.
[31] Mozia S, Borowiak-Paleń E, Przepiórski J, Grzmil B, Tsumura T, Toyoda M, et al. Physico-chemical properties and possible photocatalytic applications of titanate nanotubes synthesized via hydrothermal method. J Phys Chem Solids. Mar. 2010;71(3):263–72. doi: 10.1016/J.JPCS.2009.12.074.
[32] Tsai CC, Chen LC, Yeh TF, Teng H. In situ Sn^{2+}-incorporation synthesis of titanate nanotubes for photocatalytic dye degradation under visible light illumination. J Alloy Compd. 2013;546:95–101. doi: 10.1016/j.jallcom.2012.08.081.
[33] Feng M, You W, Wu Z, Chen Q, Zhan H. Mildly alkaline preparation and methylene blue adsorption capacity of hierarchical flower-like sodium titanate. ACS Appl Mater Interfaces. Dec. 2013;5(23):12654–62. doi: 10.1021/AM404011K.
[34] Song H, Jiang H, Liu T, Liu X, Meng G. Preparation and photocatalytic activity of alkali titanate nano materials A2TinO2n+1 (A = Li, Na and K). Mater Res Bull. Feb. 2007;42(2):334–44. doi: 10.1016/J.MATERRESBULL.2006.05.025.
[35] Vithal M, Rama Krishna S, Ravi G, Palla S, Velchuri R, Pola S. Synthesis of Cu2 + and Ag + doped Na2Ti3O7 by a facile ion-exchange method as visible-light-driven photocatalysts. Ceram Int. Sep. 2013;39(7):8429–39. doi: 10.1016/J.CERAMINT.2013.04.025.
[36] Habibi-Yangjeh A, Pournemati K. A review on emerging homojunction photocatalysts with impressive performances for wastewater detoxification. Crit Rev Env Sci Technol. 2024;54:290–320. doi: 10.1080/10643389.2023.2239125.

[37] Hemmati-Eslamlu P, Habibi-Yangjeh A. A review on impressive Z- and S-scheme photocatalysts composed of g-C3N4 for detoxification of antibiotics. FlatChem. Jan. 2024;43:100597. doi: 10.1016/J.FLATC.2023.100597.

[38] Yu C, Li G, Kumar S, Yang K, Jin R. Phase transformation synthesis of novel Ag_2O/Ag_2CO_3 heterostructures with high visible light efficiency in photocatalytic degradation of pollutants. Adv Mater. Feb. 2014;26(6):892–8. doi: 10.1002/ADMA.201304173.

[39] Dong W, Pan F, Xu L, Zheng M, Sow CH, Wu K, et al. Facile synthesis of CdS@TiO2 core–shell nanorods with controllable shell thickness and enhanced photocatalytic activity under visible light irradiation. Appl Surf Sci. Sep. 2015;349:279–86. doi: 10.1016/J.APSUSC.2015.04.207.

[40] Rezaei M, Nezamzadeh-Ejhieh A, Massah AR. A comprehensive review on the boosted effects of anion vacancy in the heterogeneous photocatalytic degradation, part I: Focus on sulfur, nitrogen, carbon, and halogen vacancies. Ecotoxicol Env Saf. Jan. 2024;269:115927. doi: 10.1016/J.ECOENV.2024.115927.

[41] Zayed M, Ahmed AM, Shaban M. Synthesis and characterization of nanoporous ZnO and Pt/ZnO thin films for dye degradation and water splitting applications. Int J Hydrog Energy. 2019;44(33):17630–48. doi: 10.1016/j.ijhydene.2019.05.117.

[42] Gao T, Li Q, Wang T. Sonochemical synthesis, optical properties, and electrical properties of core/shell-type ZnO nanorod/CdS nanoparticle composites. Chem Mater. Feb. 2005;17(4):887–92. doi: 10.1021/CM0485456.

[43] Al-Senani GM, Nasr M, Zayed M, Ali SS, Alshaikh H, Abd El-Salam HM, et al. Fabrication of PES modified by $TiO_2/Na_2Ti_3O_7$ nanocomposite mixed-matrix woven membrane for enhanced performance of forward osmosis: Influence of membrane orientation and feed solutions. Membranes. Jul. 2023;13(7):654. doi: 10.3390/MEMBRANES13070654.

[44] Josun J, Sharma P, Kumar Garg V. Optical and structural behavior of hydrothermally synthesized ZnO nanoparticles at various temperatures with NaOH molar ratios. Results Opt. Feb. 2024;14:100601. doi: 10.1016/J.RIO.2023.100601.

[45] Kumari P, Li Y, Boston R. An ionic liquid synthesis route for mixed-phase sodium titanate (Na2Ti3O7 and Na2Ti6O13) rods as an anode for sodium-ion batteries. Nanoscale. Jul. 2023;15(28):12087–94. doi: 10.1039/D3NR00639E.

[46] Lubis S, Maulana I, Sheilatina S, Mahyuni L. Preparation and photocatalytic activity of hematite from iron sand modified ZnO for indigo carmine degradation. J Phys Conf Ser. Dec. 2019;1402(5):055077. doi: 10.1088/1742-6596/1402/5/055077.

[47] Shashanka R. Investigation of optical and thermal properties of CuO and ZnO nanoparticles prepared by Crocus Sativus (Saffron) flower extract. J Iran Chem Soc. Feb. 2021;18(2):415–27. doi: 10.1007/S13738-020-02037-3.

[48] Zayed M, Samy S, Shaban M, Altowyan AS, Hamdy H, Ahmed AM. Fabrication of TiO2/NiO p-n Nanocomposite for Enhancement Dye Photodegradation under Solar Radiation. Nanomaterials. Mar. 2022;12(6):989. doi: 10.3390/NANO12060989/S1.

[49] El-Gharbawy SA, Al-Dossari M, Zayed M, Saudi HA, Hassaan MY, Alfryyan N, et al. Fabrication and characterization of nanostructured rock wool as a novel material for efficient water-splitting application. Nanomaterials. 2022;12(13):2169. doi: 10.3390/NANO12132169.

[50] Liu W, Ni J, Yin X. Synergy of photocatalysis and adsorption for simultaneous removal of Cr(VI) and Cr(III) with TiO_2 and titanate nanotubes. Water Res. Apr. 2014;53:12–25. doi: 10.1016/J.WATRES.2013.12.043.

[51] Norouzi A, Nezamzadeh-Ejhieh A, Fazaeli R. A Copper(I) oxide-zinc oxide nano-catalyst hybrid: Brief characterization and study of the kinetic of its photodegradation and photomineralization activities toward methylene blue. Mater Sci Semicond Process. Feb. 2021;122:105495. doi: 10.1016/J.MSSP.2020.105495.

[52] Mohamed WS, Hasaneen MF, Shokr EK. Influence of (Ar + O2) atmosphere and CdCl2 coating heat treatment on physical properties of CdS thin film for solar cell applications. Mater Res Express. Apr. 2017;4(4):046406. doi: 10.1088/2053-1591/AA6B7B.

[53] Alenad AM, Taha TA, Zayed M, Gamal A, Shaaban M, Ahmed AM, et al. Impact of carbon nanotubes concentrations on the performance of carbon nanotubes/zinc oxide nanocomposite for photoelectrochemical water splitting. J Electroanal Chem. Aug. 2023;943:117579. doi: 10.1016/J.JELECHEM.2023.117579.

[54] Mohamed F, Shaban M, Aljohani G, Ahmed AM. Synthesis of novel eco-friendly CaO/C photocatalyst from coffee and eggshell wastes for dye degradation. J Mater Res Technol. Sep. 2021;14:3140–9. doi: 10.1016/J.JMRT.2021.08.055.

[55] Nagaraja M, Raghu P, Mahesh HM, Pattar J. Structural, optical and Urbach energy properties of ITO/CdS and ITO/ZnO/CdS bi-layer thin films. J Mater Sci Mater Electron. Apr. 2021;32(7):8976–82. doi: 10.1007/S10854-021-05568-4.

[56] Ikhmayies SJ, Ahmad-Bitar RN. A study of the optical bandgap energy and Urbach tail of spray-deposited CdS:In thin films. J Mater Res Technol. Jul. 2013;2(3):221–7. doi: 10.1016/J.JMRT.2013.02.012.

[57] "Understanding Spectra from the Earth." https://seos-project.eu/earthspectra/earthspectra-c02-p11.html (accessed Sep. 24, 2023).

[58] Belahssen O, Ben Temam H, Lakel S, Benhaoua B, Benramache S, Gareh S. Effect of optical gap energy on the Urbach energy in the undoped ZnO thin films. Opt (Stuttg). Aug. 2015;126(15–16):1487–90. doi: 10.1016/J.IJLEO.2015.04.010.

[59] Schleuning M, Ahmet IY, van de Krol R, May MM. The role of selective contacts and built-in field for charge separation and transport in photoelectrochemical devices. Sustain Energy Fuels. Aug. 2022;6(16):3701–16. doi: 10.1039/D2SE00562J.

[60] Nezamzadeh-Ejhieh A, Karimi-Shamsabadi M. Comparison of photocatalytic efficiency of supported CuO onto micro and nano particles of zeolite X in photodecolorization of Methylene blue and Methyl orange aqueous mixture. Appl Catal A Gen. May 2014;477:83–92. doi: 10.1016/J.APCATA.2014.02.031.

[61] Salmanzadeh-Jamadi Z, Habibi-Yangjeh A, Xu C, Wang C. Anchoring Bi4O5I2 and CDs on brown TiO2−x: S-scheme heterojunction mechanism for impressive degradation of several antibiotics under visible light. J Alloy Compd. Jul. 2023;948:169711. doi: 10.1016/J.JALLCOM.2023.169711.

[62] Mohamed AS, AbuKhadra MR, Abdallah EA, El-Sherbeeny AM, Mahmoud RK. The photocatalytic performance of silica fume based Co3O4/MCM-41 green nanocomposite for instantaneous degradation of Omethoate pesticide under visible light. J Photochem Photobiol A Chem. Apr. 2020;392:112434. doi: 10.1016/J.JPHOTOCHEM.2020.112434.

[63] Abukhadra MR, Fathallah W, El Kashief FA, El-Sherbeeny AM, El-Meligy MA, Awwad EM, et al. Insight into the antimicrobial and photocatalytic properties of NiO impregnated MCM-48 for effective removal of pathogenic bacteria and toxic levofloxacin residuals. Microporous Mesoporous Mater. Jan. 2021;312:110769. doi: 10.1016/J.MICROMESO.2020.110769.

[64] Shaban M, Hamd A, Amin RR, Abukhadra MR, Khalek AA, Khan A, et al. Preparation and characterization of MCM-48/nickel oxide composite as an efficient and reusable catalyst for the assessment

of photocatalytic activity. Env Sci Pollut Res. Sep. 2020;27(26):32670–82. doi: 10.1007/S11356-020-09431-7.

[65] Ibrahim M, Zayed M, Ahmed AM, Ghanem MA, Shaban M, Abd Elkhalik S, et al. Synthesis and characterization of Mo-doped PbS thin films for enhancing the photocatalytic hydrogen production. Mater Chem Phys. Mar. 2024;315:128962. doi: 10.1016/J.MATCHEMPHYS.2024.128962.

[66] Khan I, Saeed K, Ali N, Khan I, Zhang B, Sadiq M. Heterogeneous photodegradation of industrial dyes: An insight to different mechanisms and rate affecting parameters. J Env Chem Eng. Oct. 2020;8(5):104364. doi: 10.1016/J.JECE.2020.104364.

[67] Elbadawy HA, Elhusseiny AF, Hussein SM, Sadik WA. Sustainable and energy-efficient photocatalytic degradation of textile dye assisted by ecofriendly synthesized silver nanoparticles. Sci Rep. Feb. 2023;13(1):1–13. doi: 10.1038/s41598-023-29507-x.

[68] Zha R, Nadimicherla R, Guo X. Ultraviolet photocatalytic degradation of methyl orange by nanostructured TiO2/ZnO heterojunctions. J Mater Chem A. Mar. 2015;3(12):6565–74. doi: 10.1039/C5TA00764J.

[69] Bai N, Liu X, Li Z, Ke X, Zhang K, Wu Q. High-efficiency TiO2/ZnO nanocomposites photocatalysts by sol–gel and hydrothermal methods. J Sol-Gel Sci Technol. Jul. 2021;99(1):92–100. doi: 10.1007/S10971-021-05552-8.

[70] Saeed M, Muneer M, Ul Haq A, Akram N. Photocatalysis: an effective tool for photodegradation of dyes – a review. Env Sci Pollut Res. Sep. 2021;29(1):293–311. doi: 10.1007/S11356-021-16389-7.

[71] Panthi G, Park M, Kim HY, Lee SY, Park SJ. Electrospun ZnO hybrid nanofibers for photodegradation of wastewater containing organic dyes: A review. J Ind Eng Chem. Jan. 2015;21:26–35. doi: 10.1016/J.JIEC.2014.03.044.